ARTICLE

In Situ Electron Microscopy Investigation of Sodiation of Titanium Disulfide Nanoflakes

Xiuzhen Wang,[†,‡,●] Zhenpeng Yao,[#,●] Sooyeon Hwang,[‡] Ying Pan,[¶] Hui Dong,[⊥] Maosen Fu,[§] Na Li,[∥,‡] Ke Sun,[‡] Hong Gan,[‡] Yan Yao,[⊥] Alán Aspuru-Guzik,[#,■,□,○] Qingyu Xu,[*,†] and Dong Su[*,‡]

†School of Physics, Southeast University, Nanjing 211189, China

‡Center for Functional Nanomaterials, Brookhaven National Laboratory, Upton, New York 11973, United States

#Department of Chemistry and Chemical Biology, Harvard University, Cambridge, Massachusetts 02138, United States

¶Department of Materials Science and Engineering, Massachusetts Institute of Technology, Cambridge, Massachusetts 02139, United States

⊥Department of Electrical & Computer Engineering and Materials Science and Engineering Program, University of Houston, Houston, Texas 77204, United States

§State Key Laboratory of Solidification Processing, School of Materials Science and Engineering, Northwestern Polytechnical University, Xi'an 710000, China

∥Frontier Institute of Science and Technology jointly with College of Science, State Key Laboratory for Mechanical Behavior of Materials, Xi'an Jiaotong University, Xi'an 710054, China

■Department of Chemistry and Department of Computer Science, University of Toronto, Toronto, Ontario M5S 3H6, Canada

□Vector Institute for Artificial Intelligence, Toronto, Ontario M5S 1M1, Canada

○Canadian Institute for Advanced Research (CIFAR) Senior Fellow, Toronto, Ontario M5S 1M1, Canada

S *Supporting Information*

ABSTRACT: Two-dimensional (2D) metal sulfides show great promise for their potential applications as electrode materials of sodium ion-batteries because of the weak interlayer van der Waals interactions, which allow the reversible accommodation and extraction of sodium ions. The sodiation of metal sulfides can undergo a distinct process compared to that of lithiation, which is determined by their metal and structural types. However, the structural and morphological evolution during their electrochemical sodiation is still unclear. Here, we studied the sodiation reaction dynamics of TiS_2 by employing *in situ* transmission electron microscopy and first-principles calculations. During the sodium-ion intercalation process, we observed multiple intermediate phases (phase II, phase Ib, and phase Ia), different from its lithiation counterpart, with varied sodium occupation sites and interlayer stacking sequences. Further insertion of Na ions prompted a multistep extrusion reaction, which led to the phase separation of Ti metal from the Na_2S matrix, with its 2D morphology expanded to a 3D morphology. In contrast to regular conversion electrodes, TiS_2 still maintained a compact structure after a full sodiation. First-principles calculations reveal that the as-identified phases are thermodynamically preferred at corresponding intercalation/extrusion stages compared to other possible phases. The present work provides the fundamental mechanistic understanding of the sodiation process of 2D transition metal sulfides.

KEYWORDS: titanium disulfide, sodium-ion batteries, in situ transmission electron microscopy, multistep sodiation, density functional theory
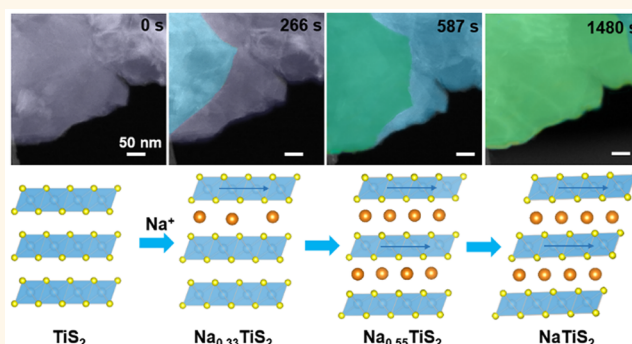
I n recent years, the Li-ion battery (LIB) industry has been continuously expanding due to the steadily increasing demands of a growing market for portable electronic devices.[1−3] Nevertheless, the rising cost and unbalanced
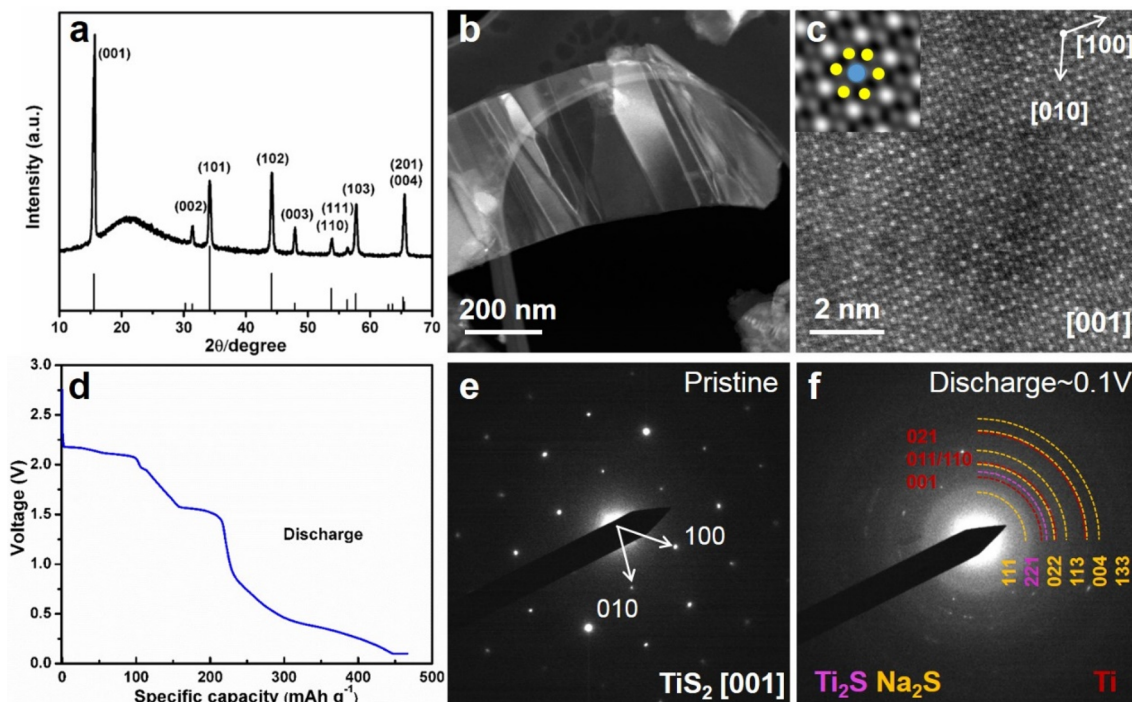
Figure 1. (a) XRD pattern of pristine TiS_2 nanoflakes. (b) HAADF-STEM image and (c) HR-STEM image of TiS_2 nanoplates seen along the [001] zone axis. The atomic model overlapping with the enlarged image is shown in the inset. Blue and yellow dots indicate Ti and S, respectively. (d) Galvanostatic discharge curve of the TiS_2 coin cell between 3.0 and 0.1 V. SAED patterns of (e) pristine single nanoflakes and (f) after discharging to 0.1 V.

geometric distribution of lithium resources make it cogent to exploit alternative energy storage systems, such as sodium-ion batteries, which are based on the earth-abundant element sodium.[4−6] Both Li and Na are alkali metal elements with similar chemical properties, which allows that the development of sodium-ion batteries (NIBs) can be benefitted greatly from the knowledge developed for LIBs.[7] However, the larger atomic radius and different electronegativity of Na ions directly affect the ion transport and storage in the electrochemical process, making some two-dimensional layered LIB electrode materials, such as graphite, unsuitable for NIBs.[8−10] Promising electrode materials for NIBs are clearly needed for further improvements.

Two-dimensional transition metal dichalcogenides (TMDs) adopt layered structures, where metal atoms are sandwiched between chalcogen atoms in a hexagonal arrangement, with neighboring layers interacting through weak van der Waals forces.[11−13] This layered structure makes TMDs insertion hosts to accommodate foreign atoms.[14,15] For example, MoS_2, SnS_2, CuS, ReS_2, $SnSe_2$, etc., recently have been extensively explored for the applications of LIBs or NIBs.[16−20] Among the TMDs, titanium disulfide (TiS_2) has a high electronic conductivity (2×10^2 S/cm at 25 °C)[21] and a wide interlayer spacing between Ti−S layers, capable of accommodating large guest cations such as Na and K ions.[22] Originally, TiS_2 was explored as a cathode material for LIBs in the 1970s, and recently it started to draw attention from the NIB field.[23,24] The Na/TiS_2 cell displayed a modest specific capacity of 188 mAh g^{-1} at 0.2 C rate and retained a reversible capacity of 170 mAh g^{-1} after 100 cycles.[25] Great efforts have been made in order to improve its rate capability and cyclability.[26,27] Despite the chemical similarity of Li and Na, reaction pathways in TiS_2 may be different because of (i) differences in ionic radius (Li$^+$:

0.76 Å, Na$^+$: 1.02 Å) and standard reduction potential (Li$^+$/Li: −3.04 V, Na$^+$/Na: −2.71 V vs standard hydrogen electrode);[7] (ii) distinct structures of stoichiometric Na-TiS_2 compounds: NaTiS_2 has $R\bar{3}m$ structure, while LiTiS_2 has $P\bar{3}m1$ structure;[28] (iii) possible trigonal prismatic coordination only possible with Na.[29] Further improvement of the performance of the TiS_2 electrode demands a comprehensive understanding of the sodiation mechanism. This challenge has motivated researchers to investigate the sodiation process using various experimental characterizations[27,30,31] and numerical simulation methods.[29,32,33]

As revealed in previous X-ray diffraction (XRD) results,[21,25,30] the sodiation of TiS_2 undergoes an intercalation process:

$$x\text{Na} + TiS_2 \rightarrow Na_xTiS_2 \ (0 < x < 1) \tag{1}$$
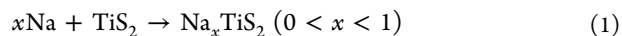
The phase transitions of the Na_xTiS_2 system were investigated via electrochemical and X-ray techniques in samples intercalated with the liquid ammonia technique, and several intermediate phases during the sodiation process were reported that are different from the lithiation process: $0.17< x < 0.33$ (II), $0.38 < x < 0.72$ (Ib), and $0.79 < x < 1$ (Ia).[31,32,34] The difference in reaction mechanism is assumed to be related to the larger ionic radius of the Na ion, which affects the bonding nature between guest ions and titanium sulfide layers. The density functional theory (DFT) calculations also showed the existence of phase Ib and phase Ia with different Na ordering in the P3 and O3 host (using the notation of Delmas) and predicted the phase transition of O1−P3 → P3 → O3 as the Na ion concentration increases, whereas previous transmission electron microscopy (TEM) studies only showed the existence of an ordered $Na_{0.25}TiS_2$ superstructure.[29,33,35−37] In-depth real-time investigations are demanded to elucidate the
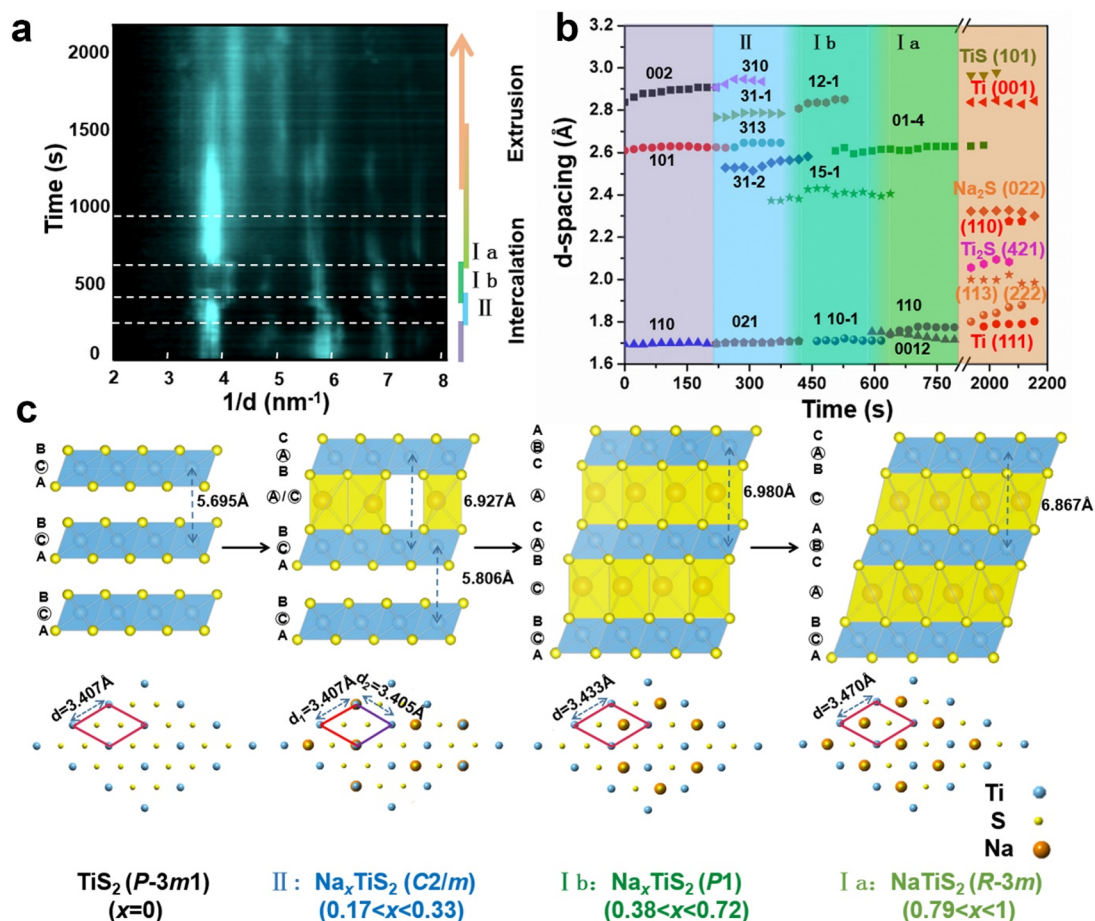
Figure 2. (a) *In situ* electron diffraction intensity profile as a function of reaction time during sodiation of TiS_2. (b) Sodium-ion-insertion-induced lattice changes measured from the TiS_2 diffraction spot during intercalation. Each symbol represents each plane. The different background color means different dominant phase: purple (pristine), blue (II), dark green (Ib), and light green (Ia). The orange background color shows the extrusion phases: Na_2S ($Fm\overline{3}m$), TiS ($R\overline{3}m$), Ti_2S ($Pnnm$), and Ti ($P6/mmm$). (c) Atomic models representing intermediate phase evolution during intercalation with different anion stacking sequences and Na configurations.

exact phase transformation and associated Na-insertion geometries of the TiS_2 host. Up to now, the dynamics of phase transitions along with the morphological and mechanical changes during sodiation are still not well understood.

In this study, we have employed an *in situ* TEM technique to investigate the structural evolution of TiS_2 nanoflakes during sodiation in real time. With *in situ* selected area electron diffraction (SAED) complemented with DFT calculations, we have identified three intermediate phases, phase II ($Na_{0.33}TiS_2$), phase Ib ($Na_{0.55}TiS_2$), and phase Ia ($NaTiS_2$), in which the sodium-occupied sites and the anion stacking sequence evolution have been elucidated with the insertion of Na ions along Ti–S layers. Combined with *in situ* scanning TEM (STEM) imaging, we observed the propagation of the phase boundary of the intermediate phases in a single flake. Our results elucidate three sequential reaction steps in the intercalation process. These intercalation reactions occur along the in-plane TiS_2 layer and do not destroy the Ti–S layered structure. Moreover, we find that further Na ions will prompt an extrusion reaction through multiple steps to produce Ti and Na_2S sequentially, as revealed by *in situ* SAED and *ex situ* high-resolution TEM. In an extrusion reaction, the morphological structure changes from two dimensions to three dimensions. Our work provides a mechanistic understanding of the

structural evolution and electrochemistry of the sodiation process of TMDs.

RESULTS AND DISCUSSION

The structure of the pristine TiS_2 nanoflakes was revealed as the hexagonal structure of 1T-TiS_2 matching JCPDS card no. 88-1967 (with a space group of $P\overline{3}m1$) by XRD (Figure 1a), without any noticeable impurity phases.[38] Figure 1b,c show a low-magnification high-angle annular dark field scanning TEM (HAADF-STEM) image and an atomic-resolution HAADF-STEM image along the [001] zone axis, respectively. The nanoflake exhibits a good crystallinity, and an atomic model with sulfur and titanium atoms is shown in the inset of Figure 1c. Figure 1d shows a galvanostatic discharge curve of TiS_2 under a constant current density of 12 mA g^{-1} in a coin cell. The initial discharge capacity reaches 450 mAh g^{-1}. Since the theoretical capacity of TiS_2 is 239 mAh g^{-1} (corresponding to 1 Na ion uptake) from the intercalation reaction process, enhanced capacity indicates more than one Na ion inserted into one chemical unit of TiS_2. The voltage profile shows two plateaus at 2.2 and 1.6 V and one slope between them, which are associated with the Na-ion intercalation into Ti–S layers.[25,26] At the end of these intercalation reactions, TiS_2 is supposed to transfer to $NaTiS_2$. Further discharge to 0.4 V
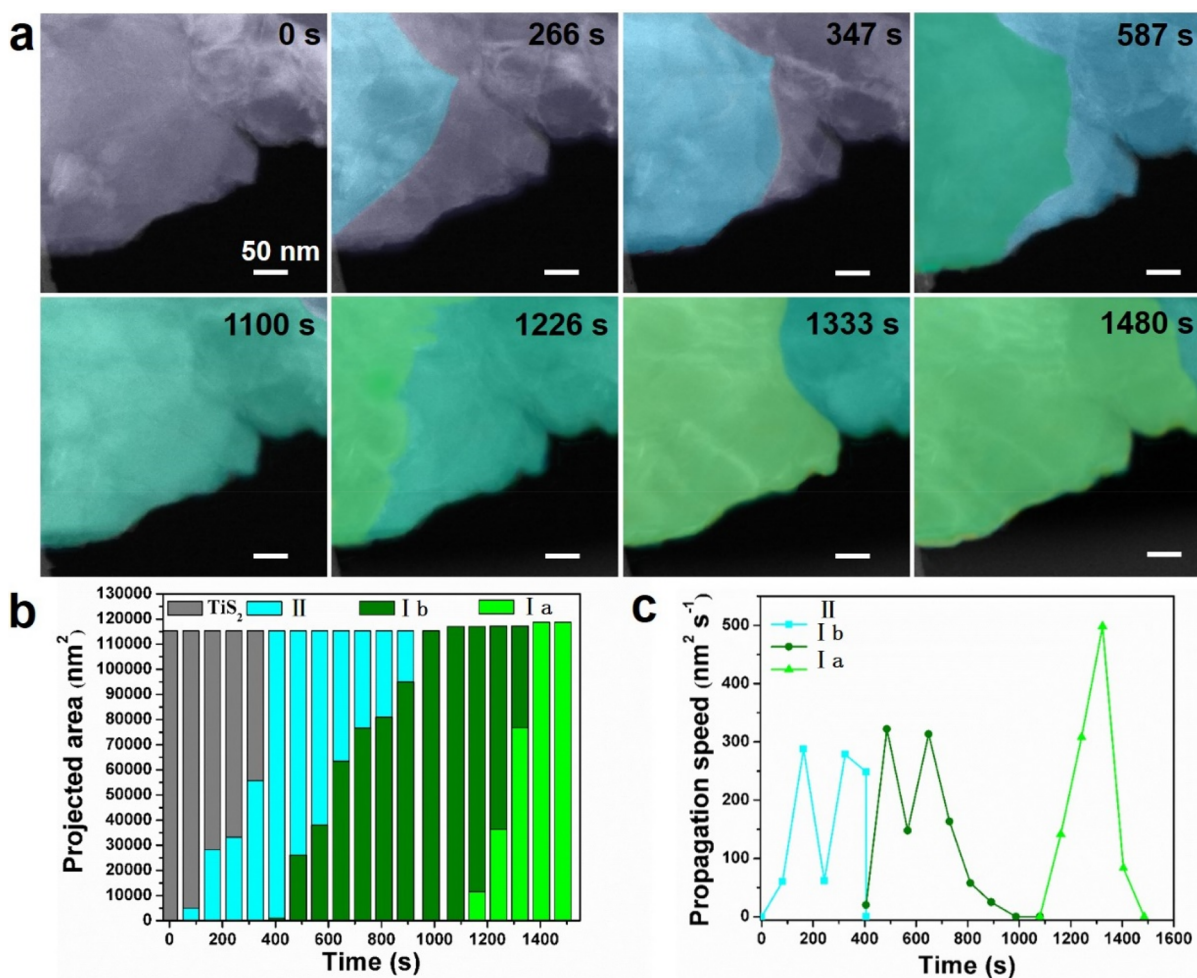
Figure 3. (a) *In situ* time-sequential dark field STEM images directly showing the movement of the phase boundary during a multistep intercalation reaction. (b) Evolution of the projected area of each intermediate phase as a function of sodiation reaction time. (c) Diffusivity of sodium ions in TiS$_2$ calculated from (a).

triggers further insertion of Na-ions, resembling an extrusion reaction resulting in the formation of metallic Ti.

This is evidenced by the comparison of SAED patterns at the pristine state (Figure 1e) and discharged state (Figure 1f), respectively. After discharging to 0.1 V, Ti and Na$_2$S phases, as well as the possible Ti$_2$S, are observed, indicating the equations

$$4Na + 2NaTiS_2 \rightarrow 3Na_2S + Ti_2S \tag{2}$$

$$2Na + Ti_2S \rightarrow Na_2S + 2Ti \tag{3}$$
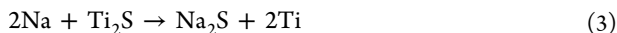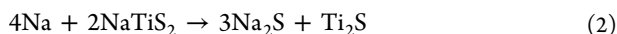
Since the theoretical capacity after the reaction (corresponding to uptake of 4 Na ions) indicated in eq 3 should be 957 mAh g^{-1}, the reaction here is not complete, as indicated from the discharge curve. The Ti$_2$S phase is supposed to be an intermediate phase. Additionally, *ex situ* high-resolution TEM (HRTEM) images and STEM-electron energy-loss spectroscopy (EELS) mapping of the discharged TiS$_2$ electrode in Figure S1 confirmed the existence of Ti and Na$_2$S phases, and the extrusion reaction occurred during full discharge to 0.1 V in the first cycle. The reversibility of electrochemical performance and the structure of the electrode after 1 cycle were characterized, as shown in Figure S2. The reversible capacity is about 250 mAh g^{-1}, and the electrode shows a TiS$_2$ phase with a uniform distribution of Ti and S elements (Figure

S2c). Real-time structural evolution of TiS$_2$ during the sodiation is integral to understand the mechanism of reaction.

To study the structural evolution of TiS$_2$ in real time, we employed the *in situ* dry-cell TEM technique,[39] which has been applied to study the phase evolution of electrode materials for batteries at atomic resolution.[40−42] Figure 2a presents the radial intensity profiles as a function of reaction time retrieved from an *in situ* SAED experiment. Raw video and SAED patterns can be found in the Supporting Information, Movie S1 and Figure S3, respectively. The intensity profiles were retrieved by integrating the intensity of a series of SAED patterns across the full 2π range along the r direction. The final intensity profile was acquired after background subtraction using a power-law model in Figure 2a. It can be seen that the intensity of Bragg reflections formed changed or disappeared in cases, indicating the phase evolution with the proceeding of sodiation. From the pristine phase to the intercalated phase, the three intermediate phases are attributed to a C2/m phase (phase II, Na$_x$TiS$_2$, 0.17 < x < 0.33), a P1 phase (phase Ib, Na$_x$TiS$_2$, 0.38 < x < 0.72), and an R$\bar{3}$m phase (phase Ia, Na$_x$TiS$_2$, 0.79 < x < 1), respectively. The *in situ* SAED here cannot quantify the amount of Na ion inserted into the system but only reflects the structural information. These phases were proposed in previous studies on TiS$_2$'s sodiation[32,43] and confirmed later in the DFT calculations of this work. Our
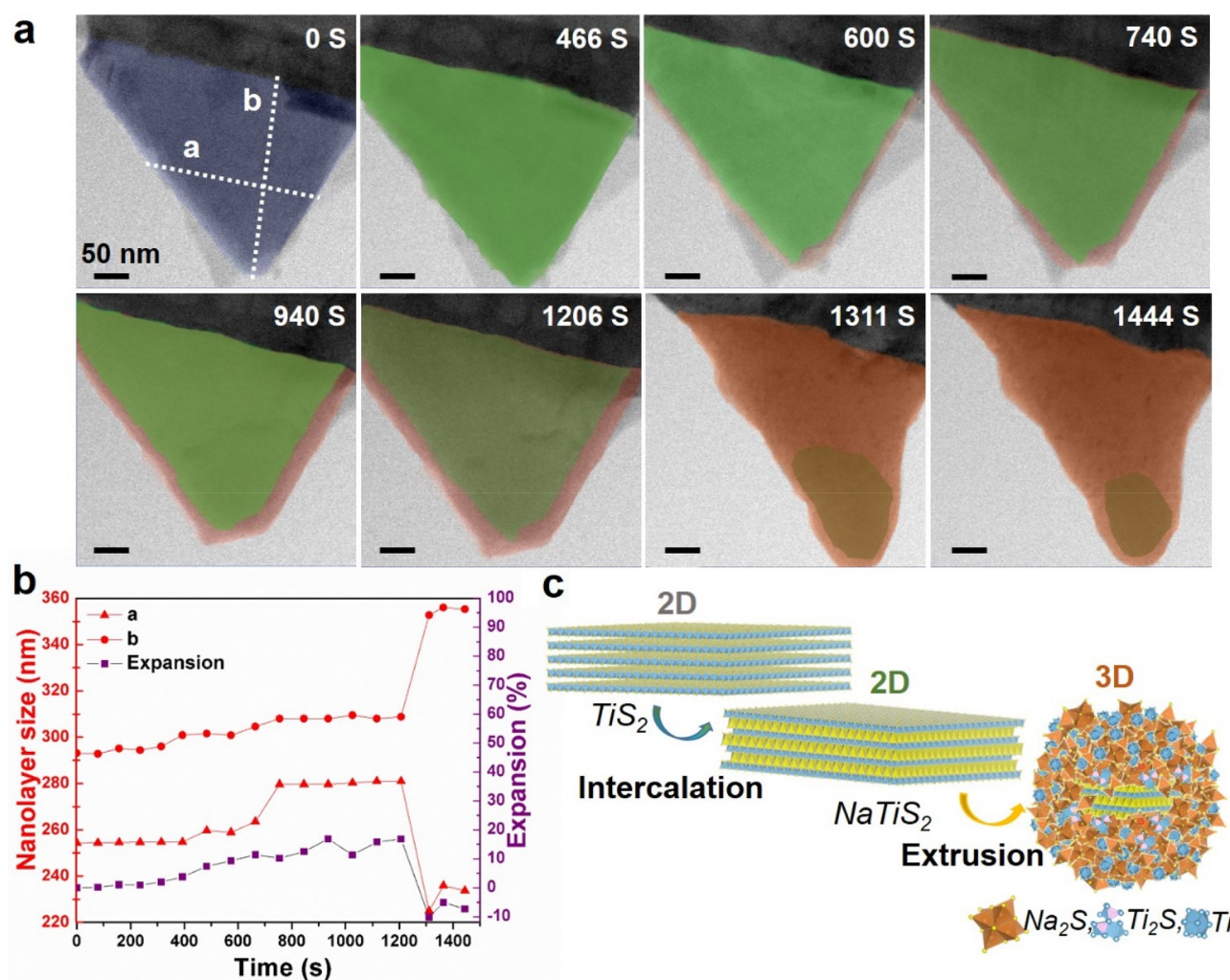
Figure 4. (a) BF-STEM images showing the whole process of phase evolution. The overlaid false colors indicate three different phases: pristine TiS$_2$ (purple), NaTiS$_2$ (light green), and Ti+Na$_2$S (orange). (b) Changes in length along two directions as a function of reaction time. (c) Model of the morphology changes from a 2D plate to 3D bulk.

results indicate that these phases can coexist while proceeding within the field of view, indicating the sodiation inhomogeneity in one nanoflake. We plotted the changes of lattice parameters as a function of reaction time based on the *in situ* SAED (Figure 2b and Figure S3). During the whole Na-ion intercalation processes, the in-plane lattice parameters changed marginally, which was consistent with a typical 2D material intercalation process. Our *in situ* SAED result of the intercalation process can be repeatedly observed from another single nanoflake as shown in Figure S4 and Movie 2. The three-step phase transition in the intercalation process was observed from the real-time investigation. Atomic models of these intermediate phases are shown in Figure 2c. The initial Na-ion intercalation prompted the phase transition from the $P\bar{3}m1$ (pristine, O1 host) phase to the $C2/m$ (phase II, O1−P3 host) phase until a nominal composition of $x = 0.17$, in which Na ions filled every two channels between Ti−S layers (stage 2), which may induce the formation of superlattice reflections.[37] Phase II (O1−P3 host) is a hybrid stacking that combines octahedral sites and trigonal prismatic sites, in which the trigonal prismatic sites are partly filled with Na ions (A or C sites), while the octahedral sites are empty. Prismatic Na-ion sites (α and β shown in Figure S5) share one face with a Ti−S octahedron directly above or directly below it, which

makes the two prismatic sites symmetrically equivalent.[33] The insertion of Na ions triggered a sliding of every other S−Ti−S layer in the host structure, and the S anion layer stacking followed a distinct AB-AB-BC-BC-CA-CA stacking mode.[35] Na-ion ordering in one layer is shown in a top-view depiction of Figure 2c, and the interlayer distance is not the same due to the Na-ion nonuniform insertion. The distance of the adjacent Ti−Ti layer with Na ions filling sites enlarged about 21%, while the Ti layer distance without Na ions expanded less than 2%. With further Na-ion insertion, the $C2/m$ phase transferred to the $P1$ (phase Ib, P3 host) phase. The phase Ib exhibits an AB-BC-CA stacking sequence of S with Na ions occupying only trigonal prismatic sites. Lithium ions in Li$_x$TiS$_2$ do not occupy trigonal prismatic sites due to their relatively smaller ionic size,[29] while Na ions with large size can stabilize the trigonal prismatic structure by reducing electrostatic repulsion between anions. With the further intercalation of Na ions, the final $R\bar{3}m$ (phase Ia, O3 host) phase is found with an AB-CA-BC anion stacking, where all the prismatic sites of Na ions are transferred to octahedral sites with the shifting of Ti−S layers, which leads to the shorter interlayer spacing along the c direction and longer spacing along the a direction. For the whole intercalation process, the cell volume was expanded about 20.5%, and each of these host structures can transform
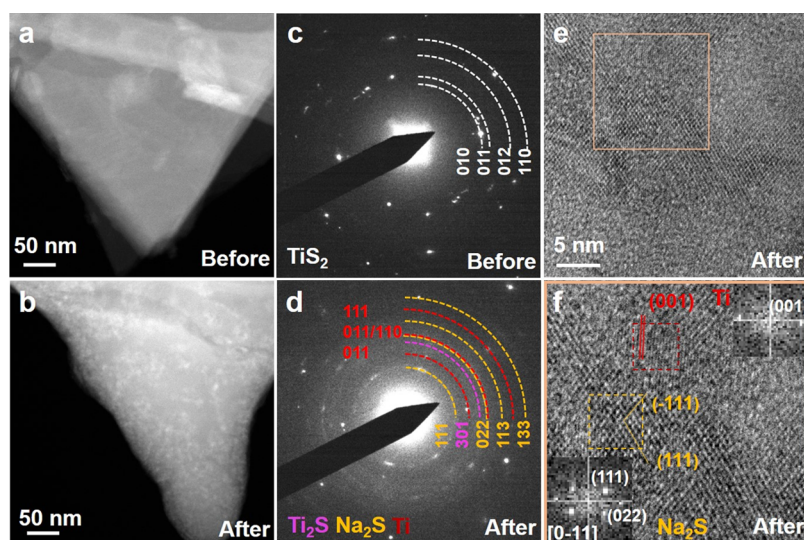
Figure 5. HAADF-STEM images of TiS_2 nanoplates showing the morphology (a) before and (b) after *in situ* sodiation and SAED patterns (c) before and (d) after, respectively. (e) HRTEM image after sodiation and (f) an enlarged image from the selected area in (e), showing the lattice patterns of Ti and Na_2S. Insets are the FFT patterns from the selected areas in (f).

into the other phase sequentially through a simple gliding of the Ti—S layers without the breaking of Ti—S bonds, as shown in Figure 2c.

After intercalation reaction processes, we found that excessive Na ions can trigger an extrusion reaction. After about 1000 s, additional reflections appeared in the electron diffraction intensity profile (Figure 2a and Figure S3), which can be attributed to the phases of Na_2S ($Fm\bar{3}m$), TiS ($R\bar{3}m$), Ti_2S ($Pnnm$), and Ti ($P6/mmm$), respectively. The coexistence of TiS, Ti_2S, and Ti implies an extrusion reaction process and an inhomogeneous degree of sodiation among the same nanoflakes. The extrusion reaction was not completed even after 2000 s, where reflections from TiS and Ti_2S were identified in the frame of 2062 s (Figure S3). This suggests that Ti separating from $NaTiS_2$ nanoflakes underwent an extrusion reaction mechanism rather than a conversion reaction. The mechanistic understanding of the morphological evolution and sodiation dynamics is a significant consideration in the design of high-performance nanostructured electrodes.

To understand the sodiation dynamics of TiS_2 in real space, an *in situ* STEM technique was applied to monitor the microstructural evolution of a single TiS_2 nanoflake upon Na-ion insertion shown in the time-lapsed images of Figure 3a. The raw annular dark-field (ADF)-STEM images and video are shown in the Supporting Information (Figure S6 and Movie 3). At 266 s, the reaction front was observed to propagate from left to right upon sodiation under a bias voltage of −4.0 V, attributed to the phase transition ($TiS_2 \rightarrow$ phase II). The second phase change was observed at 587 s along the same direction, corresponding to the transition from phase II to phase Ib. With further insertion of Na ions, the third reaction front was also observed at 1226 s, showing the abrupt change in morphology at the boundary of phases Ib and Ia. The difference in the first two steps is the serious deformation of the reaction interface (Figure S6) due primarily to the huge slippage between Ti—S—Ti layers and the expansion of Ti—Ti layers along the a and b directions. After the intercalation reaction, the pristine-layered structure shape was well maintained. The projected area changes as a function of time were measured from time-sequential STEM images during

three-step intercalation reactions (Figure 3b). As shown in Figure 3c, we can quantify the projection speed from the results of Figure 3b. The projection speed of the three phases is estimated to be 50−500 nm^2 s$^{−1}$ by calculating the projected reaction area change *versus* reaction time, based on the equation $D = \Delta S/\Delta t$, where D is the projected prolongation speed, ΔS is the change of projected reaction area, and Δt is the diffusion time. For a 2D structure, Na-ion intercalation occurs preferentially along the in-plane direction and between Ti—S slabs. Our analyses can give an estimation of the reaction kinetics, even though it varies with experimental factors, such as rate, loading, strain, and Na concentration. The low-magnification HAADF-STEM images before and after the reaction are shown in Figure S7. Sodiation reaction occurred at whole nanoflakes as volume expansion proceeds along all in-plane directions from the touch point, which further proved the reaction was not caused by electron beam radiation. In another *in situ* experiment, we observed not only the intercalation process but also the extrusion process under a higher bias voltage of −8.0 V that prompts the sodium ions to diffuse into the sample, as shown in Figure 4, Figure S8, and Movie 4. After the intercalation process, the extrusion reaction has started at 600 s and the volume expanded up to 17% at 1206 s (Figure 4b), leading to a large volume expansion. The surface became swollen, indicating the extrusion reaction front propagated forward (lateral traverse) and inward (shell-to-core). With further Na-ion diffusion, the projected area shrank and the surface bulged, indicating the two-dimensional (2D) nanoflake expanded to a three-dimensional (3D) bulk shape (Figure 4c). During the early stages of sodiation, the surface of the sample expands, and the inner sample undergoes a compressive stress. With further sodiation, the inner volume of the stressed particle expands and then induces the observed surface deformation. During the extrusion reaction process, more Na-ion insertion breaks the TiS_2 layered structure and surface swell deformation releases stress. The HAADF-STEM and SAED images before and after the *in situ* sodiation experiment are presented in Figure 5a−d. By comparing the before and after images, we can clearly see the changes. The pristine two-dimensional layered structure expanded to a three-
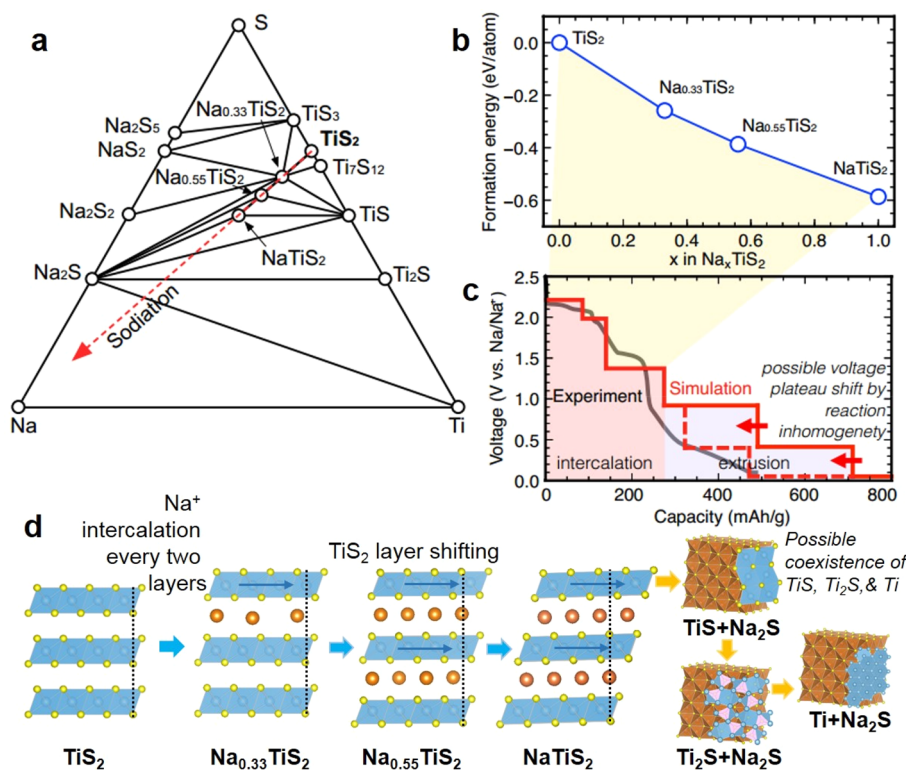
Figure 6. DFT simulation of the sodiation process in TiS$_2$ crystals. (a) Na–Ti–S phase diagram. (b) TiS$_2$–NaTiS$_2$ convex hull with sodiated TiS$_2$ intermediate phases. (c) Discharge voltage profiles as a function of Na content in Na$_x$TiS$_2$ calculated from first-principles calculation. (d) Structure evolution during the sodiation process of TiS$_2$.

dimensional bulk structure. Many small particles were formed on the surface, and their phase structure was confirmed by SAED and HRTEM. The SAED results showed the existences of Ti$_2$S, Na$_2$S, and Ti. The separation of Ti and Na$_2$S should contribute to the volume expansion and morphological structure changes. HRTEM images after sodiation are also shown in Figure 5e and f. The existence of Na$_2$S and Ti is further confirmed. The morphology and phase structure after the entire sodiation reaction are understood. We investigated here the reaction mechanism of commercial TiS$_2$ nanoflakes. There might be some kinetic differences if nanoflakes have different sizes, but the reaction mechanism revealed in this work should be applicable in most cases. All in all, the *in situ* electron diffraction and STEM imaging in this work provides us information about phase evolution and the morphological changes during the full sodiation reaction. This information is important for the mechanical modeling of a practical battery.

Phase diagrams constructed using first-principles calculations-computed energies have been broadly used to demonstrate the thermodynamic phase equilibrium of multicomponent systems and predict chemical reactions between phases.[44] Here in this study, we built the ternary Na–Ti–S phase diagram using the structures that have the lowest energy for all compositions obtained from the Inorganic Crystal Structure Database (ICSD).[45] We determined the elemental reference states (Na, Ti, S) *via* fitting[46] to experimental formation energies, which were obtained from the SGTE substance database (SSUB) and a database constructed by P. Nash *et al*.[46−50] All the calculations needed to build the Na–Ti–S phase diagram were conducted within the Open Quantum Materials Database (OQMD) framework.[51] For the compounds with partial occupancy on the Na sites (Na$_{0.33}$TiS$_2$,

Na$_{0.55}$TiS$_2$), ground state structures were identified using the NEPS method (Figures S9 and S10 in Section SI).[52] Both of these phases are predicted to be stable, validating the experimental observations (phase II and phase Ib) as shown in Figure 6a and b. The Na–Ti–S phase diagram (T = 0 K) is shown in Figure 6a, while all thermodynamically stable compounds are marked by circles. The sodiation reaction pathway of TiS$_2$ is shown as the tie-line between TiS$_2$ and Na, which goes through several intermediate phases and multiple-phase zones as shown in the ternary phase diagrams. These regions correspond to multiple sodiation reaction steps as listed in Table 1, where the capacities and average voltages of

Table 1. Thermodynamic Equilibrium Multistep Route during the Sodiation of TiS$_2$ Predicted by DFT Calculations

	reaction	capacity (mAh/g)	voltage (V)
i	TiS$_2$ + 0.33 Na → Na$_{0.33}$TiS$_2$	80	2.20
ii	+ 0.55 Na → Na$_{0.55}$TiS$_2$	133	1.93
iii	+ 1 Na → NaTiS$_2$	239	1.35
iv	+ 2 Na → Na$_2$S + TiS	479	0.90
v	+ 3 Na → 3/2Na$_2$S + 1/2Ti$_2$S	718	0.45
vi	+ 4 Na → 2Na$_2$S + Ti	957	0.03

these reaction steps are also evaluated. The full sodiation process can be divided into two periods (Figure 6c): (1) 0 < x < 1, intercalation, and (2) 1 < x < 4, extrusion, validating the experimental observations. In Figure 6c, we compare the equilibrium reaction voltage profiles calculated with DFT with the experimentally measured voltage curve. We note that the calculated equilibrium voltage profile of TiS$_2$ during the intercalation period exhibits good agreement with the

experimental sodiation curves. Meanwhile, the overall height of the computed equilibrium voltage profile of the extrusion period reasonably agrees with the experimental sodiation curve. Considering the sodiation inhomogeneity as observed in the TEM characterization, the calculated voltage profile shifts toward the low-Na content (Figure 6c). The observed early emergence of Ti_2S, Ti, and their coexistence of TiS brings forward the later reaction steps of v and vi as shown in Table 1. Predicted phase structural evolution during the sodiation process of TiS_2 (O1) is shown in Figure 6d, which is initiated (x = 0.33) with Na ion occupying the trigonal prismatic structure of every two layers. Meanwhile, the accommodation of Na ions triggers the TiS_2 layer gliding, compared to the empty layers. Further intercalations will occur between all layers (x = 0.55, 1) with the TiS_2 layers continuing to glide to realize the ordering transformation from the P3 sequence to the O3 sequence. The insertion of Na ions is supposed to be necessary for this gliding. The further sodiation process will proceed *via* extrusion reactions with the formation of TiS, Ti_2S, metallic Ti phases, and the Na_2S phase. Even a 2D to 3D morphology change was observed from the *in situ* STEM experiment, and the nanoplates still kept their structural integrity and did not decompose into the composited structure that was commonly observed in the sodiation of conversion-type oxides. A recent report indicates that the structural integrity may play an essential role in improving the cycling stability.[53] The resulting structural integrity can lead to alleviated morphological pulverization and contact failure between the active material and the binder/current collector after discharge. Enhancing the morphological integrity and therefore the electronic conductivity of electrode particles will help in improving the battery cycling stability.

CONCLUSIONS

In summary, we have investigated the sodiation mechanism of TiS_2 nanoflakes using *in situ* SAED and STEM imaging techniques, complemented with DFT calculations. The results elucidated three sequential reaction steps in the intercalation process: II, Ib, and Ia. The stacking sequences of S−Ti−S layers change with the insertion of Na^+: from the initial phase of Na_xTiS_2 (II) with O1−P3 structure when $0.17 < x < 0.33$ to the Na_xTiS_2 (Ib) phase with P3 structure when $0.38 < x < 0.72$, and then to the Na_xTiS_2 phase (Ia) with O3 structure when $0.79 < x < 1$. The extrusion reaction was also observed following the intercalation with a slower reaction speed compared to the intercalation counterpart. Morphological evolution during the whole reaction process has been thoroughly studied by *in situ* STEM images: These intercalation reactions are in-plane and will not destroy the Ti−S layered structure, whereas the morphological structure expands from two dimensions to three dimensions during the extrusion reaction. With Na ions' insertion, the inner volume of the particle continues to expand, then induces a morphology deformation. However, the electrode materials are still kept compact, which is very different from the sodiation of the conversion-type metal oxide and may help to avoid the issue of inner passivation.[54] The reaction process thoroughly studied in this work provides microscopic insights into reaction dynamics during sodiation and offers mechanistic insights for designing high-performance electrode materials for NIBs.

METHODS

Materials. We have used commercial high-purity TiS_2 (>99%) nanopowders purchased from US Research Nanomaterials.

In Situ TEM Characterization. The *in situ* TEM experimental setup was incorporated into a Nanofactory TEM-STM specimen holder, in which TiS_2 nanoflakes dispersed onto a half lacey carbon gold. TEM half-grids were analogous to the TiS_2/C electrode, Na metal was attached to a piezo-driven W probe as the counter electrode, and a thin layer of Na_2O and NaOH formed on the Na metal as the electrolyte instead of the liquid organic electrolyte. The Na was loaded onto the holder in an Ar-filled glovebox and then transferred to a TEM column using a sealed Ar bag to avoid air exposure. During the *in situ* electrochemical tests, a negative potential of 4 V or higher was applied to the TiS_2 electrode against the Na source during the sodiation process. All the *in situ* and *ex situ* TEM measurements were performed on a JEOL 2100F TEM operated at 200 kV, and supplementary *ex situ* characterization was conducted on a Hitachi HD2700C scanning transmission electron microscope operated at 200 kV and equipped with a probe aberration corrector (spatial resolution <1 Å, energy resolution 0.35 eV) and a secondary electron microscopy detector. In this work, we performed *in situ* STEM imaging at a low current intensity (0.2 pA/cm^2). The beam effect on the sample and sodium ions can be disregarded in this case, which have been tested in our previous *in situ* sodiation work.[55,56]

Battery Assembly and Testing. The composite electrodes were prepared by casting the slurry containing 80 wt % TiS_2, 10 wt % acetylene black, and 10 wt % polyvinylidene fluoride dispersed into *N*-methyl-2-pyrrolidone on a copper foil current collector. The electrodes were dried at 60 °C under vacuum for 12 h. The electrolyte is 1 M $NaClO_4$ in ethylene carbonate/dimethyl carbonate (EC:DMC = 1:1 in volume). The CR2032-type coin cells were assembled in an argon-filled glovebox with a TiS_2 electrode as the working electrode, pure Na foil as the counter electrode, a glass fiber as the separator, and 1 M $NaClO_4$ in ethylene carbonate/dimethyl carbonate (EC:DMC = 1:1 in volume) as the electrolyte. The galvanostatic charge/discharge tests were performed on a Land BT2000 battery test system at a current density of 12 mA g^{-1} in a voltage range of 3.0−0.1 V. After the electrochemical tests, the coin cells were disassembled in the Ar-filled glovebox. The cycled electrode materials were washed in DMC to eliminate the electrolyte residue and then dispersed onto a Cu grid for *ex situ* TEM characterization.

First-Principles Calculations. All the first-principles DFT calculations were conducted using the Vienna *ab Initio* Simulation Package (VASP)[44−47] within the projector augmented wave (PAW) formalism,[48] and the Perdew−Becke−Ernzerhof (PBE) approximation[49] was employed to deal with the exchange−correlation potential. A plane wave basis with a cut-off energy of 520 eV and Γ-centered *k*-meshes with a density of 8000 *k*-points per reciprocal atom were used.

The average sodiation voltage (relative to Na/Na^+) can be computed using the negative of the reaction free energy per Na added/removed, as shown in eq 4:[50]

$$V = \frac{\Delta G_f}{F \Delta N_{Na}} \tag{4}$$

where F is the Faraday constant, ΔN_{Na} is the amount of Na added/removed, and ΔG_f is the (molar) change in free energy of the reaction. Considering a two-phase reaction between Na_xMS and Na_yMS, $Na_xMS + (y − x)Na \rightarrow Na_yMS$, ΔG_f can be approximated by the total internal energies from DFT calculations neglecting the entropic contributions (0 K),

$$\Delta E = E(Na_yMS) − E(Na_xMS) − (y − x)E(Na_{metal}) \tag{5}$$

where $E(Na_xMS)$ and $E(Na_yMS)$ are the DFT energies at the respective compositions. The neglect of entropic contributions means that the sodiation voltage profiles will follow the T = 0 K ground state convex hull and consist of a series of constant voltage steps along the two-phase regions of the convex hull, separated by discontinuities that indicate the single phase compounds on the hull. It is worth mentioning here that, in practice, sodiation/desodiation do not

necessarily proceed through two-phase reactions. Thus, the calculated $T = 0$ K voltage profiles should be viewed as an approximation to the actual voltage profiles.[51] At finite temperatures (e.g., room temperature), the voltage drops in the profile become more rounded, due to entropic effects.[52]

ASSOCIATED CONTENT

Ⓢ Supporting Information

The Supporting Information is available free of charge on the ACS Publications website at DOI: 10.1021/acsnano.9b04222.

> Additional details of ex situ S/TEM, raw diffraction patterns and images, data analysis, and theoretical calculations (PDF)
>
> Movie S1: In situ electron diffraction during a whole sodiation process (AVI)
>
> Movie S2: In situ electron diffraction during the intercalation process (AVI)
>
> Movie S3: In situ STEM showing the intercalation reaction process (AVI)
>
> Movie S4: In situ STEM showing the extrusion reaction process (AVI)

AUTHOR INFORMATION

Corresponding Authors
*E-mail: xuqingyu@seu.edu.cn.
*E-mail: dongsu88@yahoo.com.

ORCID Ⓒ
Zhenpeng Yao: 0000-0001-8286-8257
Sooyeon Hwang: 0000-0001-5606-6728
Ying Pan: 0000-0002-5252-7635
Hui Dong: 0000-0003-0169-0069
Hong Gan: 0000-0001-7898-7587
Alán Aspuru-Guzik: 0000-0002-8277-4434
Dong Su: 0000-0002-1921-6683

Author Contributions
●X. Wang and Z. Yao contributed equally.

Notes
The authors declare no competing financial interest.

ACKNOWLEDGMENTS

REFERENCES

(1) Schmuch, R.; Wagner, R.; Hörpel, G.; Placke, T.; Winter, M. Performance and Cost of Materials for Lithium-Based Rechargeable Automotive Batteries. Nat. Energy 2018, 3, 267−278.

(2) Blomgren, G. E. The Development and Future of Lithium Ion Batteries. J. Electrochem. Soc. 2017, 165, A5019−A5025.

(3) Goodenough, J. B.; Kim, Y. Challenges for Rechargeable Li Batteries. Chem. Mater. 2010, 22, 587−603.

(4) Vaalma, C.; Buchholz, D.; Weil, M.; Passerini, S. A Cost and Resource Analysis of Sodium-Ion Batteries. Nat. Rev. Mater. 2018, 3, 18013.

(5) Wu, Y.; Yu, Y. 2D Material as Anode for Sodium Ion Batteries: Recent Progress and Perspectives. Energy Storage Mater. 2019, 16, 323−343.

(6) Kang, H.; Liu, Y.; Cao, K.; Zhao, Y.; Jiao, L.; Wang, Y.; Yuan, H. Update on Anode Materials for Na-Ion Batteries. J. Mater. Chem. A 2015, 3, 17899−17913.

(7) Yabuuchi, N.; Kubota, K.; Dahbi, M.; Komaba, S. Research Development on Sodium-Ion Batteries. Chem. Rev. 2014, 114, 11636−11682.

(8) Stevensa, D. A.; Dahn, J. R. The Mechanisms of Lithium and Sodium Insertion in Carbon Materials. J. Electrochem. Soc. 2001, 148, A803−A811.

(9) Udod, I. A.; Orman, H. B.; Genchel, V. K. The Sodium-Graphite System under High-Pressure Conditions: The Comparison with the Lithium-Graphite System. Carbon 1994, 32, 101−106.

(10) Palomares, V.; Serras, P.; Villaluenga, I.; Hueso, K. B.; Carretero-González, J.; Rojo, T. Na-Ion Batteries, Recent Advances and Present Challenges to Become Low Cost Energy Storage Systems. Energy Environ. Sci. 2012, 5, 5884−5901.

(11) Manzeli, S.; Ovchinnikov, D.; Pasquier, D.; Yazyev, O. V.; Kis, A. 2D Transition Metal Dichalcogenides. Nat. Rev. Mater. 2017, 2, 17033.

(12) Tan, C.; Zhang, H. Two-Dimensional Transition Metal Dichalcogenide Nanosheet-Based Composites. Chem. Soc. Rev. 2015, 44, 2713−2731.

(13) Chhowalla, M.; Liu, Z.; Zhang, H. Two-Dimensional Transition Metal Dichalcogenide (TMD) Nanosheets. Chem. Soc. Rev. 2015, 44, 2584−2586.

(14) Hazarika, S. J.; Mohanta, D.; Tripathi, A.; Kanjilal, D. Effect of Ion Irradiation on Nanoscale TiS_2 Systems with Suppressed Titania Phase. J. Phys.: Conf. Ser. 2016, 765, 012007.

(15) Kang, W.; Wang, Y.; Xu, J. Recent Progress in Layered Metal Dichalcogenide Nanostructures as Electrodes for High-Performance Sodium-Ion Batteries. J. Mater. Chem. A 2017, 5, 7667−7690.

(16) Li, Q.; Yao, Z.; Wu, J.; Mitra, S.; Hao, S.; Sahu, T. S.; Li, Y.; Wolverton, C.; Dravid, V. P. Intermediate Phases in Sodium Intercalation into MoS_2 Nanosheets and Their Implications for Sodium-Ion Batteries. Nano Energy 2017, 38, 342−349.

(17) Hwang, S.; Yao, Z.; Zhang, L.; Fu, M.; He, K.; Mai, L.; Wolverton, C.; Su, D. Multistep Lithiation of Tin Sulfide: An Investigation Using In Situ Electron Microscopy. ACS Nano 2018, 12, 3638−3645.

(18) He, K.; Yao, Z.; Hwang, S.; Li, N.; Sun, K.; Gan, H.; Du, Y.; Zhang, H.; Wolverton, C.; Su, D. Kinetically-Driven Phase Transformation during Lithiation in Copper Sulfide Nanoflakes. Nano Lett. 2017, 17, 5726−5733.

(19) Li, Q.; Xu, Y.; Yao, Z.; Kang, J.; Liu, X.; Wolverton, C.; Hersam, M. C.; Wu, J.; Dravid, V. P. Revealing the Effects of Electrode Crystallographic Orientation on Battery Electrochemistry via the Anisotropic Lithiation and Sodiation of ReS_2. ACS Nano 2018, 12, 7875−7882.

(20) Kim, S.; Yao, Z.; Lim, J. M.; Hersam, M. C.; Wolverton, C.; Dravid, V. P.; He, K. Atomic-Scale Observation of Electrochemically Reversible Phase Transformations in $SnSe_2$ Single Crystals. Adv. Mater. 2018, 30, No. e1804925.

(21) Ryu, H. S.; Kim, J. S.; Park, J. S.; Park, J. W.; Kim, K. W.; Ahn, J. H.; Nam, T. H.; Wang, G.; Ahna, H. J. Electrochemical Properties

and Discharge Mechanism of Na/TiS$_2$ Cells with Liquid Electrolyte at Room Temperature. *J. Electrochem. Soc.* **2013**, *160*, A338−A343.

(22) Wang, L.; Zou, J.; Chen, S.; Zhou, G.; Bai, J.; Gao, P.; Wang, Y.; Yu, X.; Li, J.; Hu, Y. S.; Li, H. TiS$_2$ as a High Performance Potassium Ion Battery Cathode in Ether-Based Electrolyte. *Energy Storage Mater.* **2018**, *12*, 216−222.

(23) Whittingham, M. S. Electrical Energy Storage and Intercalation Chemistry. *Science* **1976**, *192*, 1126−1127.

(24) Newman, G. H.; Klemann, L. P. Ambient Temperature Cycling of an Na-TiS$_2$ Cell. *J. Electrochem. Soc.* **1980**, *127*, 2097−2099.

(25) Liu, Y.; Wang, H.; Cheng, L.; Han, N.; Zhao, F.; Li, P.; Jin, C.; Li, Y. TiS$_2$ Nanoplates: A High-Rate and Stable Electrode Material for Sodium Ion Batteries. *Nano Energy* **2016**, *20*, 168−175.

(26) Lee, E.; Sahgong, S.; Johnson, C. S.; Kim, Y. Comparative Electrochemical Sodium Insertion/Extraction Behavior in Layered Na$_x$VS$_2$ and Na$_x$TiS$_2$. *Electrochim. Acta* **2014**, *143*, 272−277.

(27) Srimuk, P.; Lee, J.; Tolosa, A.; Kim, C.; Aslan, M.; Presser, V. Titanium Disulfide: A Promising Low-Dimensional Electrode Material for Sodium Ion Intercalation for Seawater Desalination. *Chem. Mater.* **2017**, *29*, 9964−9973.

(28) Ong, S. P.; Chevrier, V. L.; Hautier, G.; Jain, A.; Moore, C.; Kim, S.; Ma, X.; Ceder, G. Voltage, Stability and Diffusion Barrier Differences Between Sodium-Ion and Lithium-Ion Intercalation Materials. *Energy Environ. Sci.* **2011**, *4*, 3680−3688.

(29) Radin, M. D.; Van der Ven, A. Stability of Prismatic and Octahedral Coordination in Layered Oxides and Sulfides Intercalated with Alkali and Alkaline-Earth Metals. *Chem. Mater.* **2016**, *28*, 7898−7904.

(30) Hibma, T. X-Ray Study of the Ordering of the Alkali Ions in the Intercalation Compounds Na$_x$TiS$_2$ and Li$_x$TiS$_2$. *J. Solid State Chem.* **1980**, *34*, 97−106.

(31) Annie, L. S.; Danot, M.; Trichet, L.; Rouxel, J. Les Intercalaires A$_x$TiS$_2$ et A$_x$ZrS$_2$. Structure et Liaisons. (A = Li, Na, K, Rb, Cs). *Mater. Res. Bull.* **1974**, *9*, 191−198.

(32) Molinie, P.; Trichet, L.; Rouxel, J. The Na-TiS$_2$ System: A Critical Discussion of the Phase Boundaries, Structural and NMR Studies. *J. Phys. Chem. Solids* **1984**, *45*, 105−112.

(33) Vinckevičiūtė, J.; Radin, M. D.; Van der Ven, A. Stacking-Sequence Changes and Na Ordering in Layered Intercalation Materials. *Chem. Mater.* **2016**, *28*, 8640−8650.

(34) Suslov, E. A.; Bushkova, O. V.; Sherstobitova, E. A.; Reznitskikh, O. G.; Titov, A. N. Lithium Intercalation into TiS$_2$ Cathode Material: Phase Equilibria in a Li-TiS$_2$ System. *Ionics* **2016**, *22*, 503−514.

(35) Delmas, C.; Braconnier, J. J.; Fouassier, C.; Hagenmuller, P. Electrochemical Intercalation of Sodium in Na$_x$CoO$_2$ Bronzes. *Solid State Ionics* **1981**, *3*, 165−169.

(36) Delmas, C.; Fouassier, C.; Hagenmuller, P. Structural Classification and Properties of the Layered Oxides. *Physica B+C* **1980**, *99*, 81−85.

(37) Han, B.; Chen, S.; Zou, J.; Shao, R.; Dou, Z.; Yang, C.; Ma, X.; Lu, J.; Liu, K.; Yu, D.; Wang, L.; Wang, H.; Gao, P. Tracking Sodium Migration in TiS$_2$ Using *In Situ* TEM. *Nanoscale* **2019**, *11*, 7474−7480.

(38) Lin, C.; Zhu, X.; Feng, J.; Wu, C.; Hu, S.; Peng, J.; Guo, Y.; Peng, L.; Zhao, J.; Huang, J.; Yang, J.; Xie, Y. Hydrogen-Incorporated TiS$_2$ Ultrathin Nanosheets with Ultrahigh Conductivity for Stamp-Transferrable Electrodes. *J. Am. Chem. Soc.* **2013**, *135*, 5144−5151.

(39) Li, J.; Johnson, G.; Zhang, S.; Su, D. *In Situ* Transmission Electron Microscopy for Energy Applications. *Joule* **2019**, *3*, 4−8.

(40) He, K.; Zhang, S.; Li, J.; Yu, X.; Meng, Q.; Zhu, Y.; Hu, E.; Sun, K.; Yun, H.; Yang, X. Q.; Zhu, Y.; Gan, H.; Mo, Y.; Stach, E. A.; Murray, C. B.; Su, D. Visualizing Non-Equilibrium Lithiation of Spinel Oxide *via In Situ* Transmission Electron Microscopy. *Nat. Commun.* **2016**, *7*, 11441.

(41) Wang, C. M. *In Situ* Transmission Electron Microscopy and Spectroscopy Studies of Rechargeable Batteries under Dynamic Operating Conditions: A Retrospective and Perspective View. *J. Mater. Res.* **2015**, *30*, 326−339.

(42) Gao, P.; Wang, L.; Zhang, Y. Y.; Huang, Y.; Liao, L.; Sutter, P.; Liu, K.; Yu, D.; Wang, E. G. High-Resolution Tracking Asymmetric Lithium Insertion and Extraction and Local Structure Ordering in SnS$_2$. *Nano Lett.* **2016**, *16*, 5582−5588.

(43) Whangbo, M. H.; Rouxel, J.; Trichet, L. Effects of Sodium Intercalation in TiS$_2$ on the Electronic Structure of a TiS Slab. *Inorg. Chem.* **1985**, *24*, 1824−1827.

(44) Yao, Z.; Kim, S.; He, J.; Hegde, V. I.; Wolverton, C. Interplay of Cation and Anion Redox in Li$_4$Mn$_2$O$_5$ Cathode Material and Prediction of Improved Li$_4$(Mn,M)$_2$O$_5$ Electrodes for Li-Ion Batteries. *Sci. Adv.* **2018**, *4*, No. eaao6754.

(45) Belsky, A.; Hellenbrandt, M.; Karen, V. L.; Luksch, P. New Developments in the Inorganic Crystal Structure Database (ICSD): Accessibility in Support of Materials Research and Design. *Acta Crystallogr., Sect. B: Struct. Sci.* **2002**, *58*, 364−369.

(46) Grindy, S.; Meredig, B.; Kirklin, S.; Saal, J. E.; Wolverton, C. Approaching Chemical Accuracy with Density Functional Calculations: Diatomic Energy Corrections. *Phys. Rev. B: Condens. Matter Mater. Phys.* **2013**, *87*, 075150.

(47) Wang, L.; Maxisch, T.; Ceder, G. Oxidation Energies of Transition Metal Oxides within the GGA+U Framework. *Phys. Rev. B: Condens. Matter Mater. Phys.* **2006**, *73*, 195107.

(48) Stevanović, V.; Lany, S.; Zhang, X.; Zunger, A. Correcting Density Functional Theory for Accurate Predictions of Compound Enthalpies of Formation: Fitted Elemental-Phase Reference Energies. *Phys. Rev. B: Condens. Matter Mater. Phys.* **2012**, *85*, 115104.

(49) *Thermodynamic Properties of Inorganic Materials*; SGTE: Berlin, Heidelberg, 1999; pp 21−29.

(50) Nash, P. *Thermodynamic Database*; 2013; https://tptc.iit.edu/index.php/thermo-database (accessed May 29, 2018).

(51) Kirklin, S.; Saal, J. E.; Meredig, B.; Thompson, A.; Doak, J. W.; Aykol, M.; Rühl, S.; Wolverton, C. The Open Quantum Materials Database (OQMD): Assessing the Accuracy of DFT Formation Energies. *npj Comput. Mater.* **2015**, *1*, 15010.

(52) Yao, Z.; Kim, S.; Aykol, M.; Li, Q.; Wu, J.; He, J.; Wolverton, C. Revealing the Conversion Mechanism of Transition Metal Oxide Electrodes during Lithiation from First-Principles. *Chem. Mater.* **2017**, *29*, 9011−9022.

(53) Fan, X.; Hu, E.; Ji, X.; Zhu, Y.; Han, F.; Hwang, S.; Liu, J.; Bak, S.; Ma, Z.; Gao, T.; Liou, S.; Bai, J.; Yang, X.; Mo, Y.; Xu, K.; Su, D.; Wang, C. High Energy-Density and Reversibility of Iron Fluoride Cathode Enabled *via* an Intercalation-Extrusion Reaction. *Nat. Commun.* **2018**, *9*, 2324.

(54) Li, J.; Hwang, S.; Guo, F.; Li, S.; Chen, Z.; Kou, R.; Sun, K.; Sun, C.; Gan, H.; Yu, A.; Stach, E. A.; Zhou, H.; Su, D. Phase Evolution of Conversion-Type Electrode for Lithium Ion Batteries. *Nat. Commun.* **2019**, *10*, 2224.

(55) He, K.; Zhou, Y.; Gao, P.; Wang, L.; Pereira, N.; Amatucci, G. G.; Nam, K. W.; Yang, X. Q.; Zhu, Y.; Wang, F.; Su, D. Sodiation *via* Heterogeneous Disproportionation in FeF$_2$ Electrodes for Sodium-Ion Batteries. *ACS Nano* **2014**, *8*, 7251−7259.

(56) He, K.; Lin, F.; Zhu, Y.; Yu, X.; Li, J.; Lin, R.; Nordlund, D.; Weng, T. C.; Richards, R. M.; Yang, X. Q.; Doeff, M. M.; Stach, E. A.; Mo, Y.; Xin, H. L.; Su, D. Sodiation Kinetics of Metal Oxide Conversion Electrodes: A Comparative Study with Lithiation. *Nano Lett.* **2015**, *15*, 5755−5763.